Article

Stable Surface Terminations of a Perovskite Oxyhydride from First-Principles

Published as part of The Journal of Physical Chemistry virtual special issue "Emily A. Carter Festschrift".

Kristen Wang, Victor Fung, Zili Wu, and De-en Jiang*

Read Online

ACCESS | Metrics & More | Article Recommendations | SI Supporting Information

ABSTRACT: Successful synthesis of some perovskite oxyhydrides and their unique catalytic properties have recently attracted researchers' attention. However, their surface structure remains unclear. Here we identify stable surface terminations of a prototypical perovskite oxyhydride, $BaTiO_{2.5}H_{0.5}$, under catalytically relevant temperatures and pressures by using first-principles thermodynamics based on density functional theory. Five low-index facets, including (100), (010), (210), (011), and (211), and their various terminations for a total of 47 different surfaces have been examined for relative stability at different temperatures (700, 500, 300 K) and gas environments ($10^{-15} \leq P_{O_2} \leq 1$ atm, $10^{-15} \leq P_{H_2} \leq 100$ atm). The most stable ones are found to be (010)-Ba_2O_2, (210)-Ti_2O_2, and (211)-Ba_2O_4H surface terminations. These polar surfaces are stabilized by charge compensation. This work provides important insights into the stable surfaces of perovskite oxyhydrides for future studies of their catalytic properties.
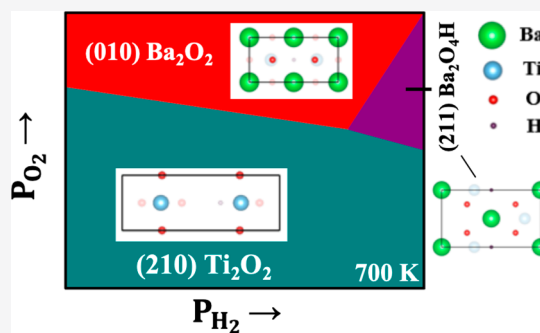
1. INTRODUCTION

Perovskite oxyhydrides are a new class of mixed anion materials derived from the extensively explored perovskite oxides of the formula ABO_3. The larger A cations are typically Ca, Sr, Ba, Na, K, Pb, La, Nd, Pr, and Ce, while the smaller B cations are typically early 3d or 4d transition metals.[1] The perovskite structure can also incorporate nonoxide anions such as H^-, and recently, it was found that the substitution of hydride anions for oxide in the $BaTiO_3$ perovskite can be successfully carried out, yielding the $BaTiO_{3-x}H_x$ perovskite oxyhydride solid with $x \leq$ 0.60.[2] These solids are interesting materials due to their labile hydrides within the solid framework[2−6] and electronic conductivity.[2,7,8]

The newly discovered $BaTiO_{3-x}H_x$ perovskite oxyhydride has found many applications in catalysis. In ammonia synthesis,[9,10] $BaTiO_{3-x}H_x$ is a more efficient support than its parent oxide, $BaTiO_3$, for the Ru metal catalyst. It is suspected that the material's labile hydrides provide a spillover pathway for the incoming H_2 required for NH_3 conversion, thus preventing the Ru metal catalyst from being poisoned.[10] The same Ru/$BaTiO_{3-x}H_x$ catalyst is also promising in CO_2 methanation.[11] Furthermore, $BaTiO_{3-x}H_x$ alone is active for ammonia synthesis as well.[9] Although some of the hydrides become replaced by nitrides, the presence of remaining labile hydrides is sufficient to continue the reaction. Likewise, the mixed oxyhydride−nitride $BaCeO_{3-x}N_yH_z$ itself acts as a catalyst for ammonia synthesis.[12] Interestingly, the $BaCeO_{3-x}N_yH_z$ catalyst can synthesize ammonia in comparable amounts to $BaTiO_{3-x}H_x$ at the same

temperature but a fifth of the pressure. This implies that a change in the B cation can have an effect on the activity of the catalyst.

The mobile hydrides within the oxyhydride framework have also been shown to be synthetically effective in the production of mixed anion material. Previously, the synthesis of $BaTiO_{2.85-y}N_{0.1}$ from $BaTiO_3$ required a temperature of 950 °C under a flow of NH_3.[13] But when $BaTiO_{2.4}H_{0.6}$ was used as a precursor, lower temperature ranges of 375−550 °C was found to be sufficient for the formation of $BaTiO_{3-x}N_{2x/3}$ with $x \leq$ 0.60.[14] At even lower temperatures of 150 °C, the $BaTiO_{2.5}H_{0.5}$ material can undergo F^-/H^- exchange to form $BaTiO_{2.5}F_{0.25}H_{0.25}$.[15,16] In contrast, prior work reports the synthesis of $BaTiO_{3-x}F_x$ from reaction of BaO_2, BaF_2, TiO_2, and Ti requiring a temperature of 1300 °C.[17]

While the recent discovery of perovskite oxyhydrides and their applications in catalysis have been exciting, the surface structure underlying their interaction with the metal catalyst and its role in catalysis are unclear. A fundamental understanding of the surface structure of perovskite oxyhydrides is therefore much needed. To the best of our knowledge, single crystals of cubic
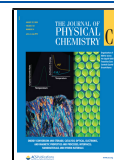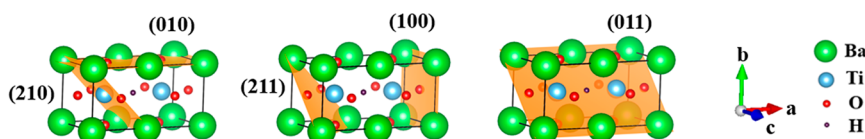
Figure 1. Models of bulk $BaTiO_{2.5}H_{0.5}$ with orange planes representing the studied cleavage direction.

$ATiO_{3-x}H_x$-type perovskite oxyhydrides are not available yet. While this prevents an experimental surface-science approach to examining their surface structure, a first-principles approach can nicely fill this gap and shed some light.

In this study, our goal is to use first-principles density functional theory to compare various surfaces and terminations of the prototypical perovskite oxyhydride, $BaTiO_{2.5}H_{0.5}$, to determine the stable surface structures relevant to catalytic conditions. These results will lay a foundation for future studies of surface chemistry and catalysis on the $BaTiO_{2.5}H_{0.5}$ perovskite oxyhydride itself as well as on $BaTiO_{2.5}H_{0.5}$-supported metal catalysts. Below, we first describe our computational methods and structural models for various surfaces and terminations of $BaTiO_{2.5}H_{0.5}$.

2. METHODS

Density functional theory (DFT) calculations were performed with Vienna *ab initio* simulation package (VASP).[18,19] Electron exchange and correlation was treated at the general-gradient approximation (GGA) level using the Perdew–Burke–Ernzerhof (PBE) functional.[20] The electron–core interactions were described by the projector augmented-wave (PAW) potentials.[21] The plane wave basis set kinetic cutoff energy was set to 450 eV. All calculations were performed with spin polarization. All models were optimized until the interatomic forces were less than 0.03 eV/Å and the total energy converged to within 10^{-5} eV. Bader charge analysis was used to obtain the partial atomic charges within the bulk and slab models.[22]

2.1. $BaTiO_{2.5}H_{0.5}$ (BTOH) Bulk Model. All surface structures studied were cleaved from the BTOH bulk. It was modeled from a $2 \times 1 \times 1$ supercell of cubic $BaTiO_3$ perovskite with a hydrogen atom replacing the central oxygen bridging between the two cubic $BaTiO_3$ unit cells. Although bulk $BaTiO_3$ is only cubic at higher temperatures but tetragonal below 400 K,[23] $BaTiO_{3-x}H_x$ of higher hydride concentrations ($\sim x = 0.6$) is in the cubic phase at room temperature.[2] So it is expected that $BaTiO_{2.5}H_{0.5}$ bulk would still be in the cubic phase. This is why we used cubic $BaTiO_3$ unit cells to construct the unit cell for the $BaTiO_{2.5}H_{0.5}$ (BTOH) bulk. The bulk structure and the five cleavage planes of focus are shown in Figure 1. The optimized lattice parameters of BTOH based on the double-cubic unit cell are $a = 8.06$ Å, $b = c = 4.03$ Å, in excellent agreement with the experimental values of $a = b = c = 4.03$ Å for BTOH based on a single cubic cell.[16]

2.2. Slab Models. A slab with two symmetrical terminations was used to model the semi-infinite surface structures of BTOH. Five low-Miller-index surfaces, including (100), (010), (210), (011), and (211), were examined (Figure 1; visualized by the VESTA program[24]). Each surface consists of a set of neutrally charged stoichiometric or nonstoichiometric terminations (see Figures S1–S5 in the Supporting Information for details). A total of 47 slab models were initially built with seven layers in each slab and, later, thicker layers were also considered for thickness-dependence; the central three layers of each slab were kept fixed to simulate the bulk region while the remaining outer

layers were relaxed. Each model was constructed with a 20 Å vacuum along the z-direction. A Monkhorst–Pack scheme[25] was used to sample the Brillouin zones: k-mesh of $3 \times 6 \times 6$ for the bulk; k-meshes of $2 \times 5 \times 1$, $5 \times 2 \times 1$, $4 \times 2 \times 1$, and $2 \times 4 \times 1$ for the (100), (010), (210), and (011)/(211) surfaces, respectively.

2.3. Surface Grand Potential. Upon cleaving the bulk, exposed surface terminations can be stabilized when in contact with an environment.[26] The resulting free energy from this interaction is quantified as the surface grand potential (SGP).[27] The SGP is plotted as a function of the surrounding gas phase's chemical potential (in our case, H_2 and O_2). Following previous work by Wang et al.,[28] the SGP of a BTOH surface termination can be written as

$$\omega_i = \frac{1}{2S}[E_{slab}^i + PV - TS - N_{Ba}\mu_{Ba} - N_{Ti}\mu_{Ti} - N_O\mu_O - N_H\mu_H] \tag{1}$$

Since DFT calculations are at 0 K and the PV term is small at reservoir pressures below 100 atm,[29] eq 1 can be rewritten as

$$\omega_i = \frac{1}{2S}[E_{slab}^i - N_{Ba}\mu_{Ba} - N_{Ti}\mu_{Ti} - N_O\mu_O - N_H\mu_H] \tag{2}$$

where ω_i is the SGP for termination i; N_{Ba}, N_{Ti}, N_O, and N_H are the number of Ba, Ti, O, and H atoms in the slab model; μ_{Ba}, μ_{Ti}, μ_O, and μ_H are the chemical potentials of Ba, Ti, O, and H atoms, and S is the surface area of termination i. The factor of $^1/_2$ is included to give the SGP per termination of the symmetric-surface slab model. The relation between the chemical potential of the bulk phase, μ_{BTOH}, and the chemical potential of each constituent element is[27]

$$\mu_{BTOH} = E_{BTOH}^{bulk} = \mu_{Ba} + \mu_{Ti} + 2.5\mu_O + 0.5\mu_H \tag{3}$$

The chemical potential term can vary with respect to the computed reference chemical potential (E)[28] as listed in Equations 4–7

$$\Delta\mu_{Ba} = \mu_{Ba} - E_{Ba}^{bulk} \tag{4}$$

$$\Delta\mu_{Ti} = \mu_{Ti} - E_{Ti}^{bulk} \tag{5}$$

$$\Delta\mu_O = \mu_O - \frac{1}{2}E_{O_2}^{gas} \tag{6}$$

$$\Delta\mu_H = \mu_H - \frac{1}{2}E_{H_2}^{gas} \tag{7}$$

where E_{Ba}^{bulk} and E_{Ti}^{bulk} are the electronic energies per atom from the optimized bulk Ba and Ti; $E_{H_2}^{gas}$ and $E_{O_2}^{gas}$ are the ground state electronic energies of an isolated H_2 and O_2 molecule, respectively. Substituting eqs 3–7 into eq 2 yields the SGP equation
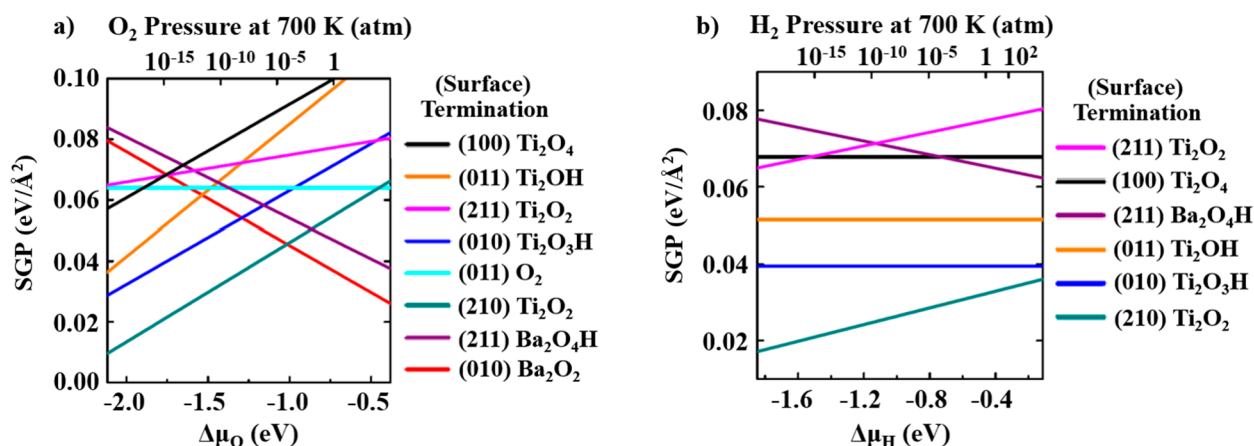
Figure 2. Relative stabilities of most stable BaTiO$_{2.5}$H$_{0.5}$ terminations at 700 K: (a) under increasing oxidation condition, with $P_{H2} = 10^{-15}$ atm and $10^{-15} \leq P_{O2} \leq 1$ atm; (b) under increasing reducing condition, with $P_{O2} = 10^{-15}$ atm and $10^{-15} \leq P_{H2} \leq 100$ atm.
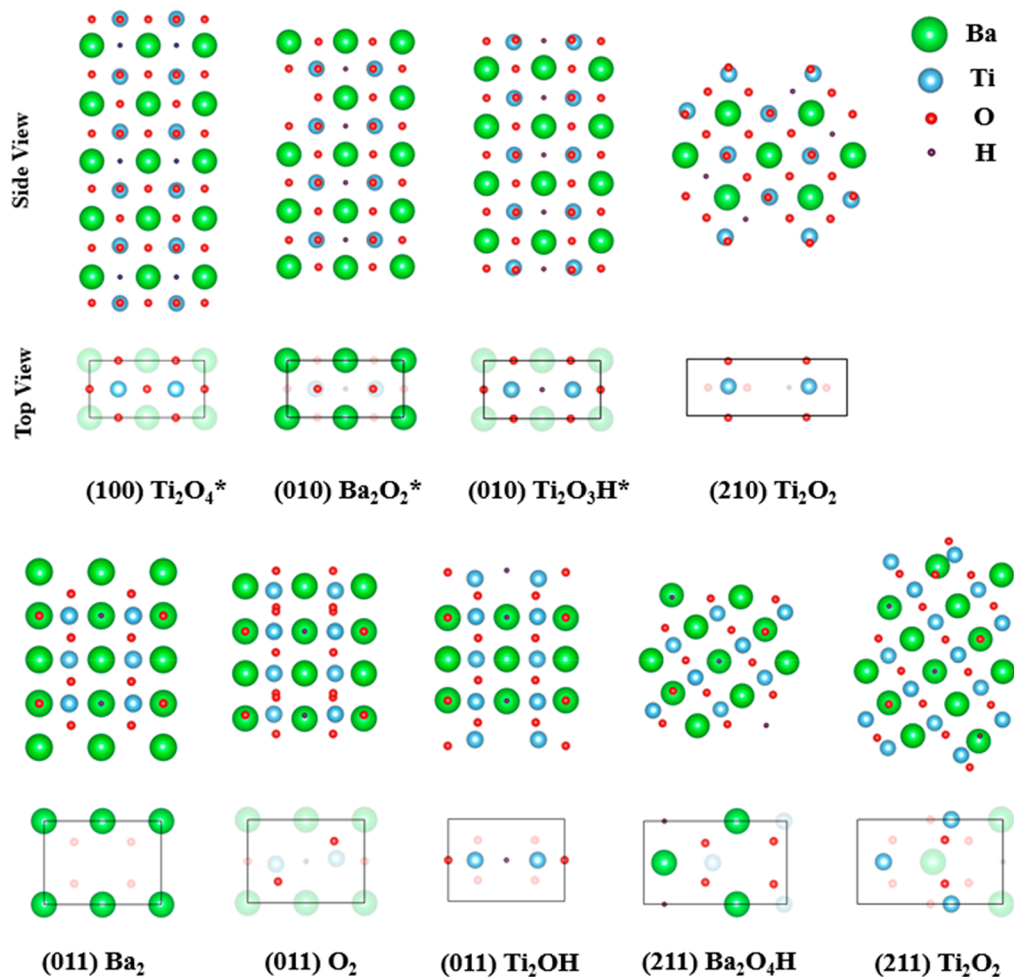

Figure 3. Side and top views of the nine most stable surface terminations of BaTiO$_{2.5}$H$_{0.5}$ after geometry optimization. Stoichiometric terminations are marked with an asterisk.

$$\omega_i = \phi_i - \frac{1}{2S}[(N_{Ba} - N_{Ti})\Delta\mu_{Ba} + (N_O - 2.5N_{Ti})\Delta\mu_O$$
$$+ (N_H - 0.5N_{Ti})\Delta\mu_H] \qquad (8)$$

where

$$\phi_i = \frac{1}{2S}\left[E_{slab}^i - N_{Ti}E_{BTOH}^{bulk} - (N_{Ba} - N_{Ti})E_{Ba}^{bulk}\right.$$
$$\left. - (N_O - 2.5N_{Ti})\frac{1}{2}E_{O_2}^{gas} - (N_H - 0.5N_{Ti})\frac{1}{2}E_{H_2}^{gas}\right]$$
$$(9)$$

Values of $\Delta\mu_H$ and $\Delta\mu_O$ corresponding to pressure ranges of $10^{-15} \leq P_{H2} \leq 100$ atm and $10^{-15} \leq P_{O2} \leq 1$ atm were
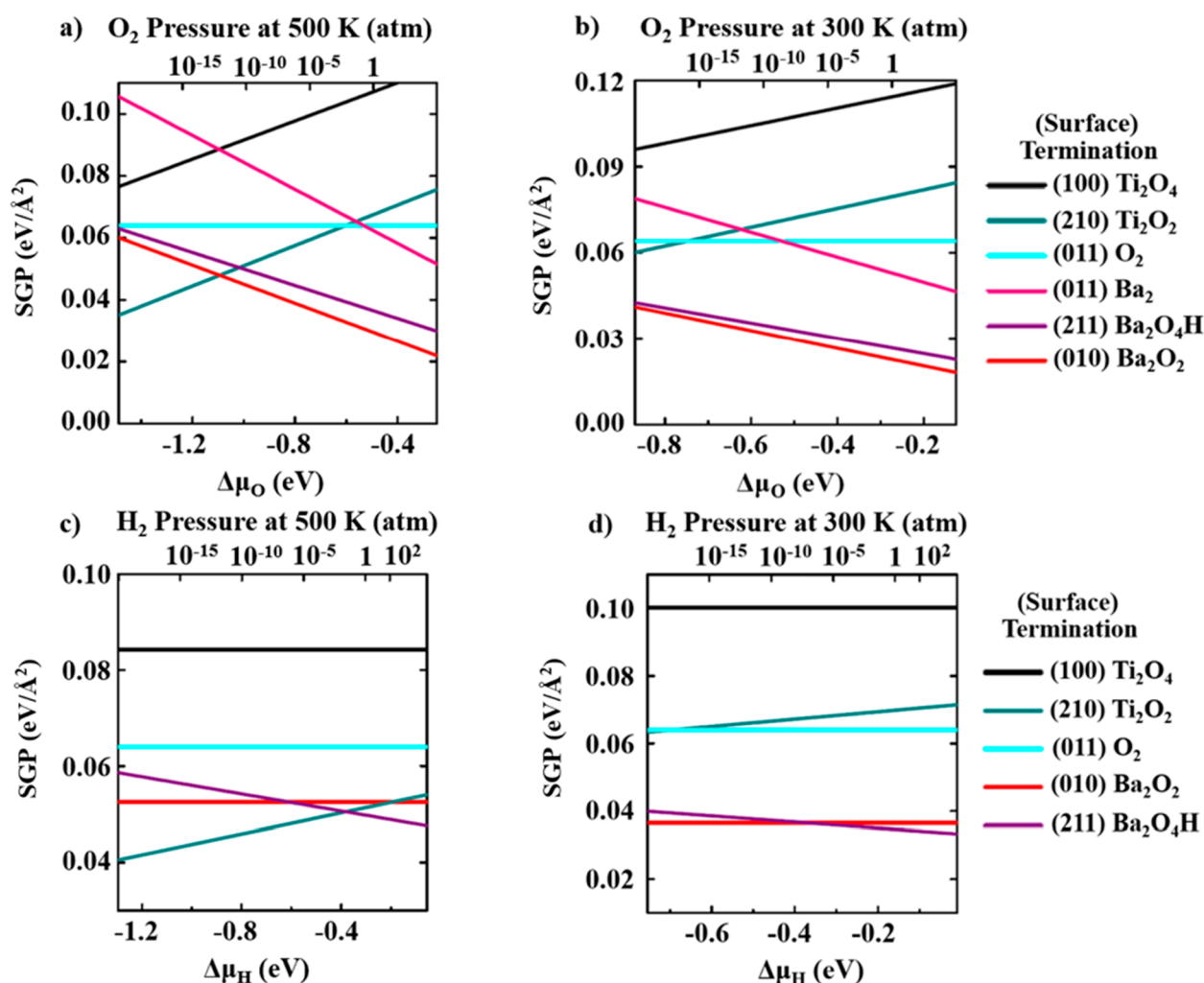
Figure 4. Relative stabilities of most stable $BaTiO_{2.5}H_{0.5}$ terminations at different temperatures: (a) 500 K and under increasing oxidation condition ($P_{H2} = 10^{-15}$ atm); (b) 300 K and under increasing oxidation condition ($P_{H2} = 10^{-15}$ atm); (c) 500 K and under increasing reducing condition ($P_{O2} = 10^{-15}$ atm); (d) 300 K and under increasing reducing condition ($P_{O2} = 10^{-15}$ atm).

considered for temperatures of 700, 500, and 300 K. In eqs 8 and 9, $\Delta\mu_{Ti}$ has been eliminated and the remaining variable, $\Delta\mu_{Ba}$, is set to -5 eV. This value was determined by setting a series of thermodynamic boundary conditions prohibiting the precipitation of other Ba-, Ti-, O-, and/or H-containing compounds on the BTOH surface. Details in calculating $\Delta\mu_{Ba}$, $\Delta\mu_{H}$, and $\Delta\mu_{O}$ values are explained in the Supporting Information.

Because Ti has localized 3d electrons, SGP calculations including the Hubbard U parameter (3.3 eV for Ti 3d) were also tested. We found that the relative surface stability trends were the same with or without the U parameter, most likely because the electrons in $BaTiO_{3-x}H_x$ form a delocalized bandstate[7] and give rise to metallic conductivity at room temperature for large enough x (>0.3).[30] Therefore, we present only the results without the U parameter for $BaTiO_{2.5}H_{0.5}$ surfaces.

As mentioned previously, the TS term in Equation 1 was ignored when calculating the SGPs for $BaTiO_{2.5}H_{0.5}$ surface at 0 K. To account for the vibrational energy and entropy contributions at finite temperatures, we estimated the effect of including the lattice vibrational energy and entropy contributions in the computation of SGPs using the harmonic approximation.[31] As shown in Figure S6 in the Supporting Information, the most stable surface terminations remain the same with or without vibrational contributions. Thus, for the

purpose of this study, finite-temperature vibrational contributions are negligible.

3. RESULTS AND DISCUSSION

3.1. Surface Stability under Varying Oxidation and Reduction Conditions at 700 K. The catalytic applications of BTOH are often at high temperatures, such as around 700 K for ammonia synthesis.[9,10] We first evaluate the surface grand potentials (SGP) at 700 K under the varying oxidation condition: $10^{-15} \leq P_{O2} \leq 1$ atm at constant $P_{H2} = 10^{-15}$ atm. A total of 47 terminations belonging to the five surfaces [(100), (010), (210), (011), and (211)] were examined and each termination was modeled by a seven-layered slab initially. The terminations with the lowest SGPs (that is, the most stable) from each surface set were remodeled with nine to 13 layers, as described in the next section, for a more accurate and converged SGP. Figure 2a plots the SGPs of these stable surface terminations to identify the overall most stable surface termination under the conditions of 700 K, $P_{H2} = 10^{-15}$ atm, and $10^{-15} \leq P_{O2} \leq 1$ atm. One can see that for $P_{O2} < 10^{-4}$ atm, the (210)-Ti_2O_2 termination is the most stable, and for $P_{O2} > 10^{-4}$ atm, the (010)-Ba_2O_2 termination is the most stable. We then evaluated the SGPs at 700 K under varying reducing
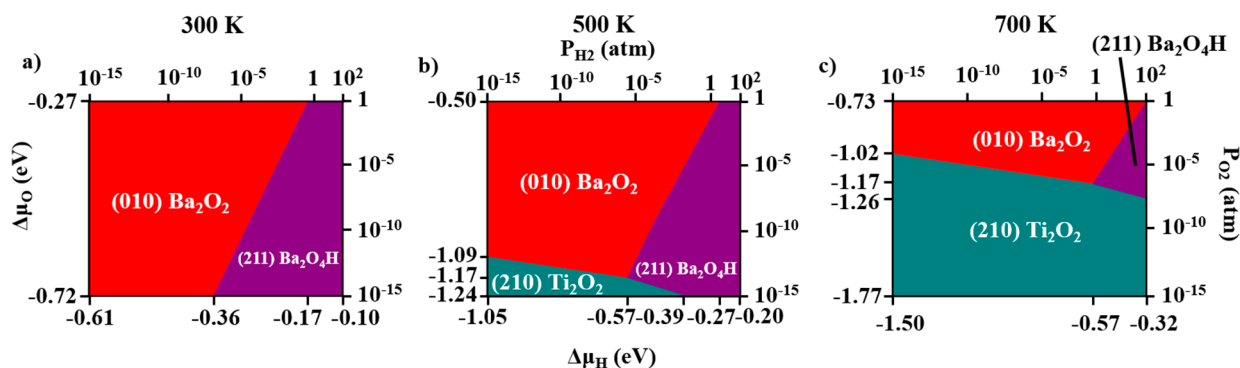
Figure 5. Surface diagrams of $BaTiO_{2.5}H_{0.5}$ as a function of O_2 and H_2 pressure (atm): (a) 300 K; (b) 500 K; (c) 700 K with $\Delta\mu_{Ba} = -5$ eV. It shows that within the given pressure boundary conditions, only the (210)-Ti_2O_2 and (010)-Ba_2O_2 surface terminations are stable at 300 K. The (210)-Ti_2O_2, (010)-Ba_2O_2, and (211)-Ba_2O_4H surface terminations are stable at 500 and 700 K.

conditions: $10^{-15} \leq P_{H2} \leq 100$ atm at constant $P_{O2} = 10^{-15}$ atm. As shown in Figure 2b, the (210)-Ti_2O_2 termination is the most stable under all H_2 pressures considered.

3.2. Structure of Stable Surface Terminations. To further confirm the surface stability, the seven-layered slabs from the most stable terminations as determined from Figure 2 were remodeled with additional layers to reach a more accurate and converged SGP.[32] As a result, we found that while nine layers were sufficient for most of the slabs, the (100)-Ti_2O_4 surface termination required 11 layers and (211)-Ti_2O_2 required 13 layers to reach SGP convergence within 0.003 eV/Å². The side and top views of the most stable, relaxed nine surface terminations with their converged number of layers are depicted in Figure 3. The surface relaxation of each slab model in Figure 3 is summarized in Table S1 of the Supporting Information.

The two most stable surface terminations from Figure 2 are (210)-Ti_2O_2 and (010)-Ba_2O_2. The relaxed (210)-Ti_2O_2 termination is a vicinal surface with a triangular-wave-like surface corrugation: the top of the triangle is a row of TiO, and the unit cell has two such rows, hence the Ti_2O_2 name; below one surface Ti atom, there are two subsurface O atoms, while below the other surface Ti atom, there is one subsurface O and one subsurface H atom. These subsurface atoms should be accessible to small adsorbates approaching the troughs of the triangular-wave-like surface corrugation of the (210)-Ti_2O_2 termination. The (010)-Ba_2O_2 termination has a rather flat surface, resembling the common A-termination of the (100) surface of a cubic ABO_3; the hydride is in the subsurface but not directly accessible to gas phase reactants, unless there is a surface oxygen vacancy for H to diffuse out to the surface.

3.3. Temperature Effects. We next examine the temperature effect on the stability under oxidation conditions. As shown in Figure 4a, the crossover from (210)-Ti_2O_2 to (010)-Ba_2O_2 in terms of stability takes place now at a much lower O_2 pressure at 500 K; in other words, lowering the temperature makes (010)-Ba_2O_2 more stable over a wider range of O_2 pressures. When the temperature is further lowered to 300 K, now the (010)-Ba_2O_2 termination becomes the most stable surface over the whole O_2 pressure range considered (Figure 4b).

In the reducing condition, and when temperature is lowered to 500 K (Figure 4c), we found that the (211)-Ba_2O_4H termination becomes the most stable when the H_2 pressure is high enough ($>10^{-2}$ atm). When temperature is further lowered to 300 K (Figure 4d), the (010)-Ba_2O_2 termination replaces the (210)-Ti_2O_2 termination as the most stable at lower H_2

pressures ($<10^{-7}$ atm). As shown in Figure 3, the relaxed surface of (211)-Ba_2O_4H is flat and exposes Ba, O, and H on the surface.

3.4. Surface Phase Diagram at Different Temperatures. Extending our stability evaluations for any given H_2/O_2 pressures at a specific temperature, we can determine the most stable surface termination at such conditions and plot the surface diagram. Figure 5 shows such surface diagrams at 300, 500, and 700 K. One can see that at 700 and 500 K there are three stable terminations: (010)-Ba_2O_2, (210)-Ti_2O_2, and (211)-Ba_2O_4H. At 300 K, there are two: (010)-Ba_2O_2 and (211)-Ba_2O_4H. Figure 5 provides a useful guide to tell the most likely surface structure of $BaTiO_{2.5}H_{0.5}$ at given temperatures and pressures of H_2 and O_2. For example, Kobayashi et al. synthesized ammonia using BTOH[9] under 5 MPa of flowing N_2/H_2 with O_2 in ppt amounts at 673 K. Figure 5c predicts that the (210)-Ti_2O_2 termination would be the most probable surface under such conditions. The present work aims to identify the stable surface terminations of $BaTiO_{2.5}H_{0.5}$ under varying temperature and pressure conditions. One can further build upon the present work's findings to investigate the $BaTiO_{2.5}H_{0.5}$ crystal morphology based on the Gibbs-Wulff theorem. Such study would be a useful one and is warranted.

3.5. Charge Compensation. Since many of the BTOH surfaces shown in Figure 3 are polar, the symmetric slabs are used to cancel the surface dipole in the supercell.[33] Here we examine the charge redistribution among the different regions of the slabs to understand the charge compensation. Equation 10 represents the general charge compensation criterion for a slab

$$\sum_{j=1}^{m} \sigma_j = -\frac{\sigma_{m+1}}{2}$$

(10)

where m is the number of relaxed outer layers each of which has a charge of σ_j, while σ_{m+1} is the charge of the central three layers of the slab (in our case) that resemble the bulk. Therefore, eq 10 states that the total charge of the m outer layers ($\sum_{j=1}^{m}\sigma_j$) must equal to negative half of the total charge of the central three bulk-like layers (σ_{m+1}) for the surface to be stabilized through charge compensation. Table 1 compares these two quantities for each slab model. One can see that all the surfaces are polar but overall the charge compensation is well maintained.

4. CONCLUSIONS

We have identified stable terminations of $BaTiO_{2.5}H_{0.5}$ surfaces under catalytically relevant temperature and pressure conditions

Table 1. Sum of Bader Charges (|e|) for the Top m Layers ($\sum_{j=1}^{m}\sigma_j$) Compared with That of the Central Three Bulk-like Layers (σ_{m+1}) for the Nine Slab Models (See Figure 3)

(surface) termination	m	$\sum_{j=1}^{m}\sigma_j$	σ_{m+1}	$-\dfrac{\sigma_{m+1}}{2}$
(100) Ti_2O_4	4	0.34	−0.72	0.36
(010) Ba_2O_2	3	0.32	−0.65	0.33
(010) Ti_2O_3H	3	−0.28	0.60	−0.30
(210) Ti_2O_2	3	2.03	−4.02	2.01
(011) Ba_2	3	2.41	−4.74	2.37
(011) O_2	3	−2.32	4.59	−2.30
(011) Ti_2OH	3	2.39	−4.8	2.40
(211) Ba_2O_4H	3	−1.93	3.88	−1.94
(211) Ti_2O_2	5	1.78	−3.52	1.76

(300−700 K, $10^{-15} \le P_{O2} \le 1$ atm, $10^{-15} \le P_{H2} \le 100$ atm) from first-principles DFT. By computing the surface grand potential, we compared 47 different terminations of $BaTiO_{2.5}H_{0.5}$ belonging to five different facets: (100), (010), (210), (011), and (211). We then constructed surface phase diagrams for different temperatures. The diagrams show that (010)-Ba_2O_2, (210)-Ti_2O_2, and (211)-Ba_2O_4H are the most stable at 700 and 500 K and that (010)-Ba_2O_2 and (211)-Ba_2O_4H are the most stable at 300 K. While (010)-Ba_2O_2 and (211)-Ba_2O_4H are flat, (210)-Ti_2O_2 is vicinal. (211)-Ba_2O_4H exposes surface hydride and (210)-Ti_2O_2 exposes subsurface hydride, but the hydride in (010)-Ba_2O_2 is not accessible. We found that charge compensation is well maintained for all of these polar surfaces. The present work has laid a foundation to further explore surface chemistry and catalysis on the surfaces of $BaTiO_{2.5}H_{0.5}$ perovskite oxyhydride.

■ ASSOCIATED CONTENT

ⓢ Supporting Information

The Supporting Information is available free of charge at https://pubs.acs.org/doi/10.1021/acs.jpcc.0c03956.

> Details in the surface relaxations; determination of the surface grand potentials; optimized geometries of bulk materials and reference states; models of all 47 $BaTiO_{2.5}H_{0.5}$ slabs belonging to the (100), (010), (210), (011), and (211) surfaces; an estimate of the lattice vibrational contribution (PDF)

■ AUTHOR INFORMATION

Corresponding Author

De-en Jiang − Department of Chemistry, University of California, Riverside, California 92521, United States; ⓞ orcid.org/0000-0001-5167-0731; Email: djiang@ucr.edu

Authors

Kristen Wang − Department of Chemistry, University of California, Riverside, California 92521, United States

Victor Fung − Center for Nanophase Materials Sciences, Oak Ridge National Laboratory, Oak Ridge, Tennessee 37831, United States; ⓞ orcid.org/0000-0002-3347-6983

Zili Wu − Center for Nanophase Materials Sciences and Chemical Sciences Division, Oak Ridge National Laboratory, Oak Ridge, Tennessee 37831, United States; ⓞ orcid.org/0000-0002-4468-3240

Complete contact information is available at:
https://pubs.acs.org/10.1021/acs.jpcc.0c03956

Notes

The authors declare no competing financial interest.

■ REFERENCES

(1) Voorhoeve, R. J. H.; Remeika, J. P.; Trimble, L. E. Defect chemistry and catalysis in oxidation and reduction over perovskite-type oxides. *Ann. N. Y. Acad. Sci.* **1976**, *272*, 3−21.

(2) Kobayashi, Y.; Hernandez, O. J.; Sakaguchi, T.; Yajima, T.; Roisnel, T.; Tsujimoto, Y.; Morita, M.; Noda, Y.; Mogami, Y.; Kitada, A.; Ohkura, M.; Hosokawa, S.; Li, Z.; Hayashi, K.; Kusano, Y.; Kim, J.; Tsuji, N.; Fujiwara, A.; Matsushita, Y.; Yoshimura, K.; Takegoshi, K.; Inoue, M.; Takano, M.; Kageyama, H. An oxyhydride of BaTiO$_3$ exhibiting hydride exchange and electronic conductivity. *Nat. Mater.* **2012**, *11*, 507−511.

(3) Tang, Y.; Kobayashi, Y.; Shitara, K.; Konishi, A.; Kuwabara, A.; Nakashima, T.; Tassel, C.; Yamamoto, T.; Kageyama, H. On Hydride Diffusion in Transition Metal Perovskite Oxyhydrides Investigated via Deuterium Exchange. *Chem. Mater.* **2017**, *29*, 8187−8194.

(4) Sakaguchi, T.; Kobayashi, Y.; Yajima, T.; Ohkura, M.; Tassel, C.; Takeiri, F.; Mitsuoka, S.; Ohkubo, H.; Yamamoto, T.; Kim, J.; Tsuji, N.; Fujihara, A.; Matsushita, Y.; Hester, J.; Avdeev, M.; Ohoyama, K.; Kageyama, H. Oxyhydrides of (Ca, Sr, Ba) TiO$_3$ Perovskite Solid Solutions. *Inorg. Chem.* **2012**, *51*, 11371−11376.

(5) Zhang, J.; Gou, G.; Pan, B. Study of Phase Stability and Hydride Diffusion Mechanism of BaTiO$_3$ Oxyhydride from First-Principles. *J. Phys. Chem. C* **2014**, *118*, 17254−17259.

(6) Eklöf-Österberg, C.; Nedumkandathil, R.; Häussermann, U.; Jaworski, A.; Pell, A. J.; Tyagi, M.; Jalarvo, N. H.; Frick, B.; Faraone, A.; Karlsson, M. Dynamics of Hydride Ions in Metal Hydride-Reduced BaTiO$_3$ Samples Investigated with Quasielastic Neutron Scattering. *J. Phys. Chem. C* **2019**, *123*, 2019−2030.

(7) Granhed, E. J.; Lindman, A.; Eklöf-Österberg, C.; Karlsson, M.; Parker, S. F.; Wahnström, G. Band vs. polaron: vibrational motion and chemical expansion of hydride ions as signatures for the electronic character in oxyhydride barium titanate. *J. Mater. Chem. A* **2019**, *7*, 16211−16221.

(8) Yajima, T.; Kitada, A.; Kobayashi, Y.; Sakaguchi, T.; Bouilly, G.; Kasahara, S.; Terashima, T.; Takano, M.; Kageyama, H. Epitaxial Thin Films of ATiO$_{3−x}$H$_x$ (A = Ba, Sr, Ca) with Metallic Conductivity. *J. Am. Chem. Soc.* **2012**, *134* (21), 8782−8785.

(9) Kobayashi, Y.; Tang, Y.; Kageyama, T.; Yamashita, H.; Masuda, N.; Hosokawa, S.; Kageyama, H. Titanium-Based Hydrides as Heterogeneous Catalysts for Ammonia Synthesis. *J. Am. Chem. Soc.* **2017**, *139*, 18240−18246.

(10) Tang, Y.; Kobayashi, Y.; Masuda, N.; Uchida, Y.; Okamoto, H.; Kageyama, T.; Hosokawa, S.; Loyer, F.; Mitsuhara, K.; Yamanaka, K.; Tamenori, Y.; Tassel, C.; Yamamoto, T.; Tanaka, T.; Kageyama, H. Metal-Dependent Support Effects of Oxyhydride-Supported Ru, Fe, Co Catalysts for Ammonia Synthesis. *Adv. Energy Mater.* **2018**, *8*, 1801772.

(11) Tang, Y.; Kobayashi, Y.; Tassel, C.; Yamamoto, T.; Kageyama, H. Hydride-Enhanced CO$_2$ Methanation: Water-Stable BaTiO$_{2.4}$H$_{0.6}$ as a New Support. *Adv. Energy Mater.* **2018**, *8*, 1800800.

(12) Kitano, M.; Kujirai, J.; Ogasawara, K.; Matsuishi, S.; Tada, T.; Abe, H.; Niwa, Y.; Hosono, H. Low-Temperature Synthesis of Perovskite Oxynitride-Hydrides as Ammonia Synthesis Catalysts. *J. Am. Chem. Soc.* **2019**, *141*, 20344−20353.

(13) Bräuniger, T.; Müller, T.; Pampel, A.; Abicht, H.-P. Study of Oxygen-Nitrogen Replacement in BaTiO$_3$ by ^{14}N Solid-State Nuclear Magnetic Resonance. *Chem. Mater.* **2005**, *17*, 4114−4117.

(14) Yajima, T.; Takeiri, F.; Aidzu, K.; Akamatsu, H.; Fujita, K.; Yoshimune, W.; Ohkura, M.; Lei, S.; Gopalan, V.; Tanaka, K.; et al. A labile hydride strategy for the synthesis of heavily nitridized BaTiO$_3$. *Nat. Chem.* **2015**, *7*, 1017−1023.

(15) Kobayashi, Y.; Hernandez, O.; Tassel, C.; Kageyama, H. New chemistry of transition metal oxyhydrides. *Sci. Technol. Adv. Mater.* **2017**, *18*, 905−918.

(16) Masuda, N.; Kobayashi, Y.; Hernandez, O.; Bataille, T.; Paofai, S.; Suzuki, H.; Ritter, C.; Ichijo, N.; Noda, Y.; et al. Hydride in BaTiO$_{2.5}$H$_{0.5}$: A Labile Ligand in Solid State Chemistry. *J. Am. Chem. Soc.* **2015**, *137*, 15315−15321.

(17) Endo, T.; Kobayashi, T.; Sato, T.; Shimada, M. High pressure synthesis and electrical properties of BaTiO$_{3-x}$F$_x$. *J. Mater. Sci.* **1990**, *25*, 619−623.

(18) Kresse, G.; Furthmüller, J. Efficiency of ab-initio total energy calculations for metals and semiconductors using a plane-wave basis set. *Comput. Mater. Sci.* **1996**, *6*, 15−50.

(19) Kresse, G.; Furthmüller, J. Efficient Iterative Schemes for Ab Initio Total-Energy Calculations Using a Plane-Wave Basis Set. *Phys. Rev. B: Condens. Matter Mater. Phys.* **1996**, *54*, 11169−11186.

(20) Perdew, J. P.; Burke, K.; Ernzerhof, M. Generalized Gradient Approximation Made Simple. *Phys. Rev. Lett.* **1996**, *77*, 3865.

(21) Blöchl, P. E. Projector Augmented-Wave Method. *Phys. Rev. B: Condens. Matter Mater. Phys.* **1994**, *50*, 17953−17979.

(22) Tang, W.; Sanville, E.; Henkelman, G. A grid-based Bader analysis algorithm without lattice bias. *J. Phys.: Condens. Matter* **2009**, *21*, 084204.

(23) Smith, M. B.; Page, K.; Siegrist, T.; Redmond, P. L.; Walter, E. C.; Seshadri, R.; Brus, L. E.; Steigerwald, M. L. Crystal Structure and the Paraelectric-to-Ferroelectric Phase Transition of Nanoscale BaTiO$_3$. *J. Am. Chem. Soc.* **2008**, *130*, 6955−6963.

(24) Momma, K.; Izumi, F. VESTA 3 for three-dimensional visualization of crystal, volumetric and morphology data. *J. Appl. Crystallogr.* **2011**, *44*, 1272−1276.

(25) Monkhorst, H. J.; Pack, J. D. Special points for Brillouin-zone integrations. *Phys. Rev. B: Solid State* **1976**, *13*, 5188−5192.

(26) Xie, Y.; Yu, H.; Zhang, G.; Fu, H.; Sun, J. First-Principles Investigation of Stability and Structural Properties of the BaTiO$_3$ (110) Polar Surface. *J. Phys. Chem. C* **2007**, *111*, 6343−6349.

(27) Bottin, F.; Finocchi, F.; Noguera, C. Stability and electronic structure of the (1 × 1) SrTiO$_3$ (110) polar surfaces by first-principles calculations. *Phys. Rev. B: Condens. Matter Mater. Phys.* **2003**, *68*, 035418.

(28) Wang, Y.; Cheng, J.; Behtash, M.; Tang, W.; Luo, J.; Yang, K. First-principles studies of polar perovskite KTaO$_3$ surfaces: structural reconstruction, charge compensation, and stability diagram. *Phys. Chem. Chem. Phys.* **2018**, *20*, 18515−18527.

(29) Reuter, K.; Scheffler, M. Composition, structure, and stability of RuO$_2$ (110) as a function of oxygen pressure. *Phys. Rev. B: Condens. Matter Mater. Phys.* **2001**, *65*, 035406.

(30) Bouilly, G.; Yajima, T.; Terashima, T.; Yoshimune, W.; Nakano, K.; Tassel, C.; Kususe, Y.; Fujita, K.; Tanaka, K.; Yamamoto, T.; et al. Electrical Properties of Epitaxial Thin Films of Oxyhydrides ATiO$_{3-x}$H$_x$ (A = Ba and Sr). *Chem. Mater.* **2015**, *27*, 6354−6359.

(31) Fultz, B. Vibrational thermodynamics of materials. *Prog. Mater. Sci.* **2010**, *55*, 247−352.

(32) Fiorentini, V.; Methfessel, M. Extracting convergent surface energies from slab calculations. *J. Phys.: Condens. Matter* **1996**, *8*, 6525−6529.

(33) Noguera, C. Polar oxide surfaces. *J. Phys.: Condens. Matter* **2000**, *12*, R367.